Retinal blood flow speed quantification at the capillary level using temporal autocorrelation fitting OCTA [Invited]

YUNCHAN HWANG,[1] JUNGEUN WON,[1] ANTONIO YAGHY,[2] HIROYUKI TAKAHASHI,[1,2] JESSICA M. GIRGIS,[2] KENNETH LAM,[2] SIYU CHEN,[1] ERIC M. MOULT,[1] STEFAN B. PLONER,[3] ANDREAS MAIER,[3] NADIA K. WAHEED,[2] AND JAMES G. FUJIMOTO[1,*]

[1]*Department of Electrical Engineering and Computer Science, Research Laboratory of Electronics, Massachusetts Institute of Technology, Cambridge, MA 02139, USA*
[2]*New England Eye Center, Tufts Medical Center, Boston, MA 02116, USA*
[3]*Pattern Recognition Lab, Friedrich-Alexander-Universität Erlangen-Nürnberg, Erlangen, Germany*
[*]*jgfuji@mit.edu*

Abstract: Optical coherence tomography angiography (OCTA) can visualize vasculature structures, but provides limited information about blood flow speed. Here, we present a second generation variable interscan time analysis (VISTA) OCTA, which evaluates a quantitative surrogate marker for blood flow speed in vasculature. At the capillary level, spatially compiled OCTA and a simple temporal autocorrelation model, $\rho(\tau) = \exp(-\alpha\tau)$, were used to evaluate a temporal autocorrelation decay constant, α, as the blood flow speed marker. A 600 kHz A-scan rate swept-source OCT prototype instrument provides short interscan time OCTA and fine A-scan spacing acquisition, while maintaining multi mm^2 field of views for human retinal imaging. We demonstrate the cardiac pulsatility and assess repeatability of α measured with VISTA. We show different α for different retinal capillary plexuses in healthy eyes and present representative VISTA OCTA in eyes with diabetic retinopathy.

1. Introduction

The retina has specialized inner retinal and choroidal vasculature as well as dynamic retinal blood flow regulation to meet its high metabolic demand [1,2]. In retinal diseases, abnormal expression of cytokines and angiogenic factors can disrupt the retinal vasculature, which can lead to macular edema and neovascularization [3–6]. Retinal blood flow speeds have been characterized to study both normal flow regulation and flow alterations associated with pathologies [7–10]. Blood flow speed measurements in capillaries, where oxygen and metabolic substrate exchange occurs, may provide valuable and unique biomarkers to facilitate understanding of normal physiology and pathologies in retina.

Adaptive optics (AO) provides exceptional transverse resolution for in vivo retinal imaging and allows direct measurements of capillary blood flow speeds [11]. AO has been used to study cardiac pulsatility, range of speed and response to stimulation in capillaries and has deepened our understanding of hemodynamics in retinal vasculature [12–16]. However, AO provides limited field of views (FOVs) and requires a montage to acquire multi mm^2 FOV, which can be time-consuming. Doppler optical coherence tomography (OCT) is another imaging modality that directly measures blood flow speeds [8,17]. However, Doppler OCT is challenging when blood cell velocity is nearly orthogonal to the beam as in retinal capillaries, while multi-beam Doppler OCT can be used to partly overcome this issue [18,19]. OCT with repeated A-scans (M-mode) has been used to characterize flow speeds using temporal autocorrelation, by acquiring >100 A-scan repeats at each position with a temporal resolution of <100 μs [20–23]. Large numbers

of data points were fitted to various temporal autocorrelation models to determine flow speeds. However, OCT protocols with a high number of repeats are not suitable for multi mm^2 FOV human retinal imaging in a clinical setting.

Both OCT and OCT angiography (OCTA) are standard, commercially available imaging modalities in ophthalmology [24–27]. OCTA generates contrast from time-varying OCT signals, by acquiring two or more repeated B-scans separated by a given time interval (interscan time). Since OCTA is generated from OCT images which have intrinsic depth resolution, it can visualize individual retinal plexuses with great detail [28]. OCTA can detect capillary non-perfusion, neovascularization and microaneurysms (MAs) [29–32]. OCTA derived biomarkers, such as vessel density, non-perfusion area, foveal avascular zone area, have been extensively studied to characterize retinal pathologies using both commercial devices and research prototypes [33–36]. However, OCTA in its traditional form provides only structural information on vasculature and does not evaluate blood flow speeds.

Increases in OCT A-scan rates enabled extensions of OCTA for characterizing retinal blood flow speeds. The OCTA signal saturates when longer interscan times are used and blood flow speed governs how fast the saturation occurs [22]. By comparing OCTA signals measured with two different interscan times, acquired with >2 B-scan repeats, our group previously developed variable interscan time-analysis (VISTA) OCTA using a 400 kHz A-scan rate vertical cavity surface emitting laser (VCSEL) light source [37]. Relative blood flow speeds were mapped to a false color image using the ratio of en face OCTA signals measured with two different interscan times [38]. Using VISTA OCTA, we qualitatively characterized flow variations associated with age-related macular degeneration (AMD), diabetic retinopathy (DR) and polypoidal choroidal vasculopathy (PCV) [37,39–42].

Here, we introduce a next generation VISTA algorithm, which evaluates the temporal autocorrelation decay constant in human retinal vasculature at the individual capillary segment level. Higher A-scan rate (600 kHz) swept-source OCT (SS-OCT) enables multiple B-scan repeats with short interscan times and fine A-scan spacing, providing OCTA measurements at multiple interscan times and resolving retinal capillaries. We evaluate the temporal autocorrelation decay constant, α, by fitting the OCTA measurements to a simple model $\rho(\tau) = \exp(-\alpha\tau)$. We propose α (ms^{-1}) as a quantitative surrogate marker for blood flow speeds, assuming that higher blood flow speed will lead to faster autocorrelation decay and higher α. Instead of using >100 repeated A-scans, we computationally identify retinal capillary segments and compile OCTA measurements across voxels comprising each capillary segment. Here, we show that α measured from VISTA OCTA demonstrates pulsatility consistent with previous AO studies of capillary blood flow and propose a pulsatility compensation algorithm. We recruited healthy subjects and patients with diabetic retinopathy. We evaluated repeatability of VISTA α measurements at multiple spatial levels as well as consistency of α measurements from OCTA protocols with different interscan times and A-scan spacings. We also develop VISTA methods for choroidal vasculature, whose structure is distinct from inner retinal vasculature. We demonstrate that VISTA OCTA can resolve different blood flow speeds for different retinal capillary plexuses in healthy subjects and flow alterations in diabetic retinopathy patients.

2. Methods

2.1. System description and imaging acquisition

2.1.1. SS-OCT system

A retinal SS-OCT prototype instrument operating at 600 kHz A-scan rate was developed using a custom micro-electromechanical systems VCSEL (MEMS-VCSEL, Praevium Research) with a 1050 nm center wavelength and ~100 nm sweep bandwidth. The frequency sweep was linearized in time to improve SNR over the wavenumber span and more effectively utilize digitizer

bandwidth. The OCT signal and a Mach Zehnder interferometer (MZI) calibration signal were sampled simultaneously using two balanced photodetectors (PDB481C-AC, Thorlabs) and a 12-bit digitizer (ATS9373, AlazarTech) at 2 Gs/s. The MZI signal was used to resample the corresponding OCT signal to compensate sweep-to-sweep variation of the VCSEL. The incident power at the pupil was <5 mW, consistent with American National Standards Institute ocular exposure guidelines [43]. The $1/e^2$ beam diameter at pupil was 1.4 mm. A dual axis galvanometer (6210 H, Cambridge Technology) was used to scan the OCT beam on the retina. Refractive error of the eye was corrected using an electrically focus tunable liquid lens (EL-10-30-C-NIR-LD-MV, Optotune) placed before the galvanometer, without translating the OCT optics. The focus tunable liquid lens was controlled by software provided by the manufacturer (Lens Driver Controller, Optotune).

2.1.2. Human imaging and OCTA protocols

Healthy normal subjects and diabetic retinopathy patients were imaged at the New England Eye Center of Tufts Medical Center (Boston, MA). Only healthy normal subjects were imaged at Massachusetts Institute of Technology (Cambridge, MA). The study was approved by Tufts Medical Center Institutional Review Boards and Massachusetts Institute of Technology Committee on the Use of Humans as Experimental Subjects. Written informed consent was obtained before imaging. Two different scan protocols were used. Parameters of the protocols are shown in Table 1. The fundamental interscan time refers to the time interval between sequentially repeated B-scans.

Table 1. OCTA protocols

FOV	Fundamental interscan time	A-scan spacing	B-scan repeats	Scanner duty cycle	A-scans/B-scan	B-scans	Acquisition time
[a]3 mm × 3 mm	1 ms	6.7 μm	8	0.75	450	450	3.60 s
5 mm × 5 mm	1.25 ms	8.8 μm	5	0.76	570	570	3.57 s

[a]Data presented in Fig. 5 was acquired with a slightly modified 3 mm × 3 mm protocol: 0.83 ms interscan time, 7.5 μm A-scan spacing, 10 B-scan repeats, 0.8 duty cycle, 400 A-scans /B-scan, 400 B-scans, 3.33 s acquisition time.

2.2. OCTA processing and segmentation

2.2.1. OCTA acquisition

N repeated B-scans having a fundamental interscan time Δt can provide OCTA with *N*-1 different effective interscan times from Δt to $(N\text{-}1)\Delta t$. Unnormalized OCTA and normalized OCTA at $M\Delta t$ interscan time were generated from OCT signals using the following formula:

$$\text{OCTA}_{\text{unnormalized}}(M\Delta t) = \frac{1}{L(N-M)} \sum_{i=1}^{L} \sum_{j=1}^{N-M} |S^i_{j+M} - S^i_j|$$
$$\text{OCTA}_{\text{normalized}}(M\Delta t) = \frac{1}{L(N-M)} \sum_{i=1}^{L} \sum_{j=1}^{N-M} \frac{(S^i_{j+M}-S^i_j)^2}{(S^i_{j+M})^2+(S^i_j)^2}$$

(1)

S^i_j is j^{th} repeated measurement of OCT signal measured with i^{th} split spectrum [44]. *L* is the number of split spectra. Here we used 3 Gaussian spectral bands in order to better match axial and transverse resolution and reduce noise, with the adjacent Gaussian bands crossing each other at 64% of the peaks.

Eye movement during imaging was corrected by registering the unnormalized OCTA B-scan from each position to the unnormalized OCTA B-scan at the previous position using rigid translation [45]. This inter B-scan registration significantly improved connectivity of retinal vasculature. The inter B-scan registered OCTA and OCT data was then segmented.

2.2.2.   Retinal layer segmentation

The retinal pigment epithelium (RPE) was segmented for each B-scan using the structural OCT B-scan. Then, the RPE location was smoothed over the volume using 2D local regression smoothing (MATLAB fit function with lowess option, with 'Span' corresponding to $500\,\mu m \times 500\,\mu m$). The OCT and OCTA volumes were flattened with respect to the RPE. Then, three additional retinal layers were segmented: the internal limiting membrane (ILM), posterior of retinal nerve fiber layer (RNFL) and center of inner nuclear layer (INL). Simple algorithms using thresholding and peak detection were used to generate preliminary segmentation of the three layers. The segmentation results were then manually inspected and corrected over the volume. During the manual correction phase, a reader provided rough guidance on the layer location in the volume, and the local maximum of "the feature" near the given guidance was detected as the layer. The features for identifying the three layers were intensity increase along axial direction for ILM, intensity decrease along axial direction for posterior of RNFL, and low intensity for center of INL. Note that the most hypo-reflective location in the INL was approximated to be the center of INL. The manually corrected segmentation was smoothed by 2D local regression smoothing (MATLAB fit function with lowess option). The 'Span' option of ILM and center of INL corresponded to $150\,\mu m \times 150\,\mu m$ and $300\,\mu m \times 300\,\mu m$, respectively. The thickness of the RNFL was smoothed with the 'Span' corresponding to $1000\,\mu m \times 1000\,\mu m$. The RNFL posterior was located by offsetting the smoothed RNFL thickness from the smoothed ILM. The segmentation of the three retinal layers was done using the RPE-flattened structural OCT volume, Gaussian filtered with a sigma of 1 pixel axially ($2.7\,\mu m$ in tissue) and 3×3 pixels transversely.

Accurate and consistent segmentation of the RPE is crucial for choroidal vasculature segmentation. In order to fine tune the RPE segmentation, the posterior local intensity peak in Bruch's membrane-RPE complex was detected from the RPE-flattened structural OCT volume, which was Gaussian filtered in the transverse direction (sigma 3×3 pixels). The resulting fine RPE segmentation was median filtered with a window size of $200\,\mu m \times 200\,\mu m$ and used as the reference for the choroidal vasculature segmentation shown in Fig. 5.

2.2.3.   Vasculature segmentation

The three segmented inner retinal layers divided the four inner retinal plexuses into three categories: RNFL plexus (RNFLP), superficial capillary plexus + intermediate capillary plexus (SCP + ICP) and deep capillary plexus (DCP). The RNFLP region was between $19\,\mu m$ posterior to the ILM and posterior to the RNFL. The posterior shift from the ILM excluded regions with specular reflections and thin RNFL, which are reported to be avascular [46]. The SCP + ICP region was between the posterior of the RNFL and center of the INL. The DCP region was between the center of the INL and $80\,\mu m$ anterior to the RPE.

2.3.   *Temporal autocorrelation fitting*

2.3.1.   OCTA and temporal autocorrelation decay

The temporal autocorrelation of OCT and OCTA, and their relationship to blood flow dynamics have been studied extensively [20–23]. Here we provide a brief overview of the relationship between normalized OCTA and temporal autocorrelation decay. OCT signal from a voxel at x at time t can be separated into static and dynamic components, $S(x,\ t) = S_{static}(x) + S_{dynamic}(x,\ t)$, where the expected value of $S_{dynamic}$, $E[S_{dynamic}]$, is zero. In the retinal vasculature, $S_{dynamic}$ mainly arises from moving red blood cells. Treating $S(x,\ t)$ as a wide-sense stationary process over a time window that is significantly shorter than the cardiac cycle, the expected value of the squared difference of OCT acquired with interscan time τ is $E[|S(x,\ t+\tau)\text{-}S(x,\ t)|^2] = 2(\text{Var}[S_{dynamic}] - R_{dynamic}(\tau))$, where $R_{dynamic}(\tau)$ is the autocorrelation function of $S_{dynamic}(x,\ t)$. Note $\text{Var}[S_{dynamic}]$ equals $R_{dynamic}(\tau = 0)$. The expected value of the square of

the OCT signal is $E[|S(x, t)|^2] = |S_{static}|^2 + Var[S_{dynamic}]$. We define $A(\tau)$ as the scaled ratio of these two quantities [Eq. (2)] [47]:

$$
\begin{aligned}
A(\tau) &= \frac{1}{2} \frac{E[|S(x, t + \tau) - S(x, t)|^2]}{E[|S(x, t)|^2]} \\
&= \frac{Var[S_{dynamic}]}{|S_{static}|^2 + Var[S_{dynamic}]}(1 - \frac{R_{dynamic}(\tau)}{R_{dynamic}(\tau = 0)}) = \beta(1 - \rho(\tau))
\end{aligned}
\tag{2}
$$

$\beta = Var[S_{dynamic}]/(|S_{static}|^2 + Var[S_{dynamic}])$ models the ratio of dynamic versus static contribution to the signal, and $\rho(\tau) = R_{dynamic}(\tau)/R_{dynamic}(\tau = 0)$ models the normalized autocorrelation (autocorrelation coefficient) decay of the dynamic signal. The portion of the dynamic signal contribution is modeled by β and not $\rho(\tau)$. Blood flow velocity will govern how fast the autocorrelation $\rho(\tau)$ decays. Note that the OCTA$_{normalized}$ formula in Eq. (1) is sampling the ratio of squared difference of the OCT signal to the sum of square of the OCT signal at two time points. Therefore, OCTA$_{normalized}$ can be treated as sampling of $A(\tau)$ at discrete interscan times $\tau = \Delta t, 2\Delta t, \ldots (N - 1)\Delta t$, in which case β is saturated value of the OCTA$_{normalized}$.

Here, we adopted a simple model, $\rho(\tau) = \exp(-\alpha\tau)$, where α is a temporal autocorrelation decay constant. We assume a monotonic relationship between α and blood flow speeds in retinal capillaries (Discussion 4.2), and propose α as a blood flow speed surrogate marker.

2.3.2. Using spatial compilation to increase sampling and characterize temporal autocorrelation decay

The stochastic nature of blood flow means that a large number of samples are necessary for robust temporal autocorrelation decay characterization. In M-mode acquisitions, the large sampling is achieved with >100 repeated A-scans and temporal resolution of <100 μs. However, OCT protocols with >100 repeated scans require long imaging times, which are not feasible for clinical retinal imaging. Using OCTA protocols with a significantly fewer number of repeats (<10) compared with M-mode, we obtain large number of samples by spatial compilation of OCTA measurements over a spatial domain where blood flow speeds are expected to be uniform.

For inner retinal vasculature, AO studies have shown that the blood flow speeds in capillaries can change significantly (>2×) at bifurcation points [14,15], making individual capillary segments the largest spatial domain where uniform blood flow speeds can be assumed. Therefore, we spatially compile OCTA measurements over each capillary segment and evaluate a temporal autocorrelation decay constant for individual capillary segments. Note that alternate spatial domains for compilation can be adopted to study different vasculatures such as choriocapillaris / choroidal vasculature or focal vascular lesions.

2.4. VISTA pipeline for inner retinal vasculature

2.4.1. Voxel level capillary identification

In order to spatially compile the OCTA measurements for each capillary segment, voxel locations for every individual capillary segment need to be identified. Voxel level capillary identification was achieved by assigning unique identifiers (ID) during pixel level capillary identification, and then projecting these capillary IDs on the 3D vessel mask (Fig. 1(A)). First, the Hessian based vesselness response proposed by Jerman et al. was applied on the en face OCTA [48]. The global Otsu threshold from the logarithm of the vesselness response was used to produce a 2D vessel mask. The 2D vessel mask was skeletonized and turned into a graph, where the links represent center lines of the vessel and the nodes represent bifurcation points [49]. All 2D vessel pixels of the en face OCTA were given a corresponding vessel ID, visualized by different colors of segments in Fig. 1(A) (middle). The vessel ID of each pixel was projected on the corresponding

3D vessel mask, giving each voxel the vessel ID. Acquisition of the 3D vessel mask is explained in (Methods 2.5).
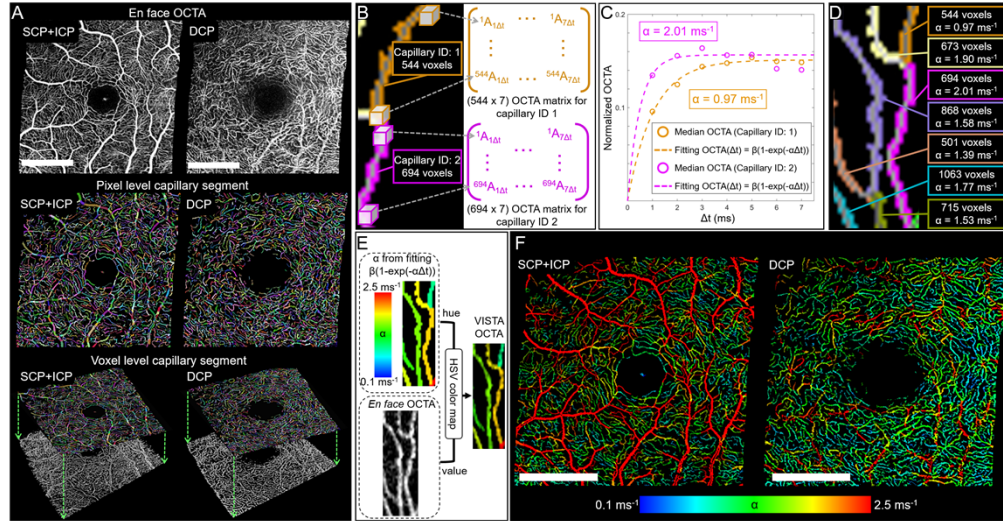

Fig. 1. VISTA pipeline for temporal autocorrelation decay (α) evaluation at the capillary level. (A) Voxel level capillary identification. En face OCTA (top) is transformed to a 2D graph (middle). The capillary ID from the 2D graph is projected on a 3D vessel mask (bottom), and is implemented separately for SCP + ICP and DCP. (B) Spatial compilation of normalized OCTA. The spatially compiled OCTA of each capillary can be represented with an OCTA matrix. (C) Temporal autocorrelation decay (α) evaluation of two capillaries shown in (B). (D) Number of voxels and corresponding α in the capillaries. (E) Visualization scheme using an HSV colormap to generate VISTA OCTA. (F) VISTA OCTA of SCP + ICP and DCP. Scale bars: 1 mm

2.4.2. Spatial compilation of OCTA measurements and OCTA matrix

Voxel level capillary identification enabled compilation of normalized OCTA measurements for each capillary segment. Compiled normalized OCTA measurements of a capillary segment, comprised of M voxels imaged with N B-scan repeats, can be represented with an $M \times (N-1)$ OCTA matrix (Fig. 1(B)), since N B-scan repeats provide OCTA at $(N-1)$ different interscan times. Medians of the normalized OCTA matrix columns, corresponding to $(N-1)$ interscan time points, were fitted to $\text{OCTA}_{\text{normalized}}(\tau) = \beta\,(1 - \exp(-\alpha\tau))$ to evaluate the temporal autocorrelation decay constant, α, of the capillary (Fig. 1(C)). The MATLAB fit function was used with 'Weights' option $[(N-1), (N-2), \dots\ 1]$, following the number of OCT pairs used for OCTA computation at each interscan time. Figure 1(D) shows the number of voxels comprising the capillary segments and their corresponding α.

2.4.3. Visualization

In order to visualize the blood flow speed surrogate marker α in en face OCTA, an HSV colormap (Hue, Saturation, Value) was used, following our previous VISTA implementation (Fig. 1(E)) [38]. The median filtered (window size: 5×5 pixels) α between $[0.1\,\text{ms}^{-1}, 2.5\,\text{ms}^{-1}]$ was linearly mapped to hue between $[0.67, 0]$, which corresponds to [blue, red]. En face OCTA from unnormalized OCTA was used for value in HSV. Saturation was set to 1. For visualization purposes, the square root of en face OCTA was used for inner retinal vasculature, due to the high

dynamic range of unnormalized OCTA. Note that the hue was determined by normalized OCTA (and its saturation characteristics) while the value was determined by unnormalized OCTA.

2.5.   *3D vessel mask for inner retinal vasculature*

The 3D vessel mask was acquired using Optimally Oriented Flux (OOF) [50]. Given a radius r, the OOF response of a voxel at x are three eigenvalues (λ_1, λ_2, λ_3, where $|\lambda_1| \geq |\lambda_2| \geq |\lambda_3|$) that quantify the image intensity gradient across the surface of the sphere of radius r along three orthogonal vectors. For example, voxels comprising a planar structure (assuming darker background) will have one large negative eigenvalue with its vector orthogonal to the plane, and two small eigenvalues with two other vectors parallel to the plane, if the radius is comparable to a half of the plane thickness. Voxels comprising a tubular structure will have two large negative eigenvalues with vectors orthogonal to the tube axis and one small eigenvalue with a vector parallel to the tube axis. We used the OOF response proposed by Law and Chung [50], with unnormalized OCTA as input:

$$M(x, r) = \begin{cases} \sqrt{|\lambda_1(x,r)\lambda_2(x,r)|} & \text{, if } \lambda_1, \lambda_2 \leq 0 \\ 0 & \text{, otherwise} \end{cases}. \qquad (3)$$

The radius of the OOF response was set to twice the A-scan spacing. This choice of radius was made to avoid identifying noise as vessels. Note that diameters of human retinal capillaries are smaller than the expected transverse point spread function (PSF) of OCT. The Otsu threshold was applied on the logarithm of the OOF volume as the global threshold to produce a 3D vessel mask.

Figure 2 shows the OOF response of the unnormalized OCTA, with depth color encoded and a vessel mask of the DCP volume. The OOF response suppresses the OCTA projection artifacts because the shape of projection artifacts is planar, making voxels corresponding to projection artifacts have only one large negative eigenvalue, while top voxels corresponding to real vessels have two large negative eigenvalues (Fig. 2(A) arrows). Thick superficial vessels are mostly removed in the DCP mask, shown in the Fig. 2(C). Cross sectional views of the OOF response show three distinct plexuses (SCP, ICP and DCP), with axially oriented, short vessels interconnecting the plexuses (Fig. 2(D) arrows).
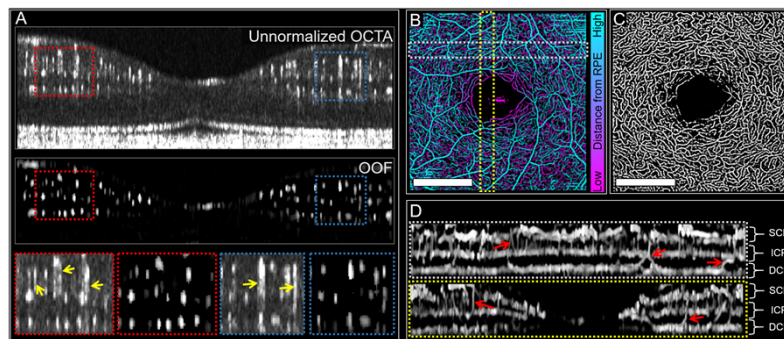

Fig. 2. Optimally Oriented Flux (OOF) for a 3D vessel mask. (A) Unnormalized OCTA B-scan (top) and corresponding OOF response (middle). Enlarged views (bottom) show OOF suppresses projection artifacts in unnormalized OCTA (yellow arrows). (B) En face, depth color-coded OOF. (C) DCP 3D vessel mask from the OOF in (B). (D) Cross sectional views of OOF response. Axially oriented interconnecting vessels are marked with red arrows. Scale bars: 1 mm

2.6. VISTA in choroidal vasculature

Since the choriocapillaris and choroid have complex vascular networks that include lobular structures as well as thick vessels, choroidal vasculature does not have a single distinct spatial domain, such as capillary segments in inner retinal vasculature, where we can assume uniform blood flow speed and compile OCTA measurements for evaluating α. Therefore, we adopted a rectangular cuboid (53 μm × 53 μm in transverse plane and 8 μm in axial direction) as the spatial domain for OCTA measurements compilation for choroidal vasculature. Note that a different size cuboid or other vascular structures can be used for the spatial domain if a specific layer of the choroidal vasculature is of interest.

2.7. Pulsatility and pulsatility compensation in VISTA

Measurements of blood flow speed or a surrogate marker over a several second acquisition time will be subject to pulsatile flow variation due to the cardiac cycle. In OCTA acquisition, where multiple B-scan repeats are acquired before the next B-scan, the pulsatility is encoded mainly in the slow scan direction, with the B-scan indices. While the pulsatility itself can be an important biomarker, it is desirable to develop techniques which compensate pulsatility in order to simplify studies involving blood flow speed quantification or visualization. For example, pulsatile variations in blood flow speed can complicate studies if alterations caused by pathology are comparable to the pulsatile effects.

2.7.1. Modeling and compensating cardiac cycle pulsatility

Pulsatility of the temporal autocorrelation decay constant α at the capillary segment level can be modeled by introducing a time varying scale factor:

$$\alpha^{(i)}(t) = \alpha_0^{(i)}(1 + g^{(i)}(t)), \text{ with } \overline{g^{(i)}(t)} = 0. \tag{4}$$

$\alpha_0^{(i)}$ is the time-averaged temporal autocorrelation decay constant of a capillary segment (i). The cardiac cycle pulsatility is modeled with a pulsatility scale factor $g^{(i)}(t)$. A pulsatility compensation scheme aims to retrieve $\hat{\alpha}_0^{(i)} = \alpha^{(i)}/(1 + \hat{g}^{(i)})$, where $\alpha^{(i)}$ is the temporal autocorrelation decay constant evaluated without pulsatility compensation and $\hat{g}^{(i)}$ is the estimated pulsatility scale factor at the time the capillary was imaged.

2.7.2. Pulsatility in VISTA measurements

To characterize the pulsatility of α measured with VISTA, the same B-scan location through the fovea of a healthy subject was repeatedly imaged for 2 seconds with 1 ms interscan time (2000 B-scans of 3 mm length with 450 A-scans/B-scan). This data is essentially an OCT volume which encodes time along one axis (marked yellow in Fig. 3(A)). Eye movement was corrected using unnormalized OCTA, therefore cross sections of vessels appear as tubular structures aligned to the time axis. OOF was applied to generate a 3D vessel mask. Roughly 50 capillary cross sections were selected and each cross section was tracked along the time axis, shown as different color tubes in Fig. 3(A). With a 100 ms time window, OCTA at interscan times from 1 ms to 7 ms were compiled and fitted to $\text{OCTA}_{\text{normalized}}(\tau) = \beta (1 - \exp(-\alpha\tau))$. By sliding the 100 ms time window along the time axis, we evaluated the time evolution of $\alpha(t)$ of each capillary and corresponding $g(t)$. Figure 3(B) shows the time evolutions of the pulsatility scale factors $g(t)$ of the segmented capillaries. The pulsatility scale factors for the capillaries show a certain degree of synchronization, but have both phase and magnitude heterogeneity. In general, the pulsatility factors have fast rise followed by slow recovery, similar to the pulsatile modulation of blood flow speeds in retinal capillaries reported in AO studies [13–15].
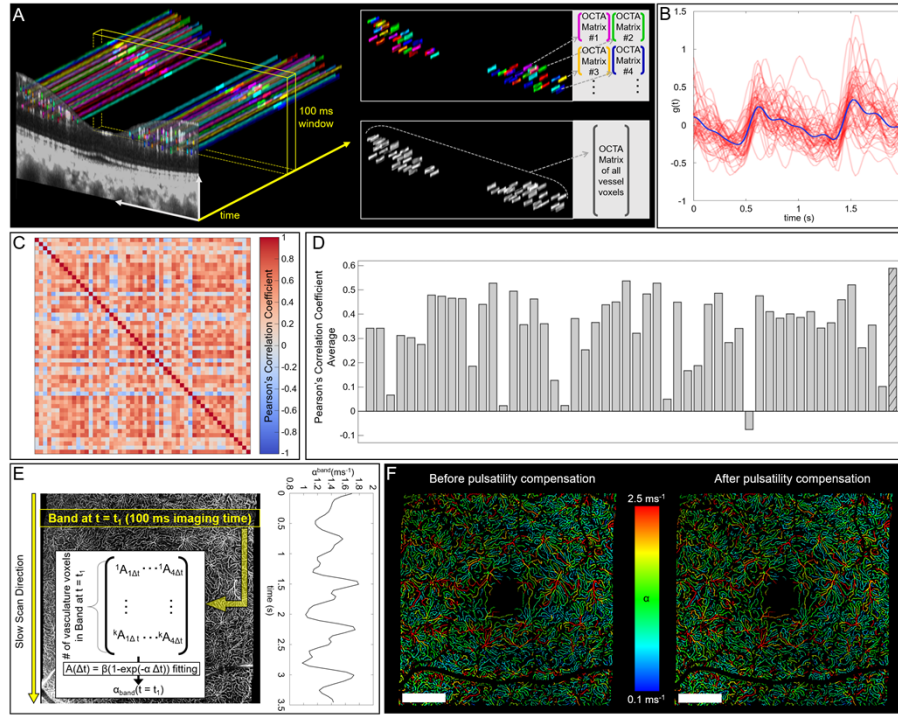
Fig. 3. Pulsatility and pulsatility compensation in VISTA. (A) Repeated B-scans at the same location over time. Compilation of OCTA in the 100 ms time window for α evaluation of the individual capillaries (top right) and the compiled vasculature (bottom right). (B) Pulsatility scale factors, $g(t)$, of individual capillaries (red) and compiled vasculature (blue). (C) Pearson's correlation coefficient matrix between pulsatility scale factors $g(t)$. The right most column is the compiled vasculature. (D) The average of Pearson's correlation coefficient with other capillaries. The right most bar (patterned) is the compiled vasculature. (E) Extracting representative pulsatility from isotropic FOV OCTA protocols. The plot on right shows the changes in α^{band} over slow scan direction, demonstrating clear pulsatility. (F) VISTA OCTA before pulsatility compensation (left) and after pulsatility compensation (right). The plot in (E) is also aligned with the VISTA OCTA images in (F). Scale bars: 1 mm

2.7.3. Representative pulsatility from compiling all vessel voxels

Here, we propose a method to extract representative pulsatility, which can be later extended to pulsatility compensation in VISTA OCTA protocols with isotropic FOVs. First, we compiled the OCTA measurements of all vessel voxels in the 100 ms time window, treating all the vessel voxels as one compiled vasculature (Fig. 3(A)). Then we evaluated the time evolution of α for the compiled vasculature, $\alpha^{\text{compiled}}(t)$ by sliding the time window along the time axis. Since the compiled vasculature includes all capillaries, the pulsatility of the compiled vasculature can serve as the representative pulsatility, $g^{\text{rep}}(t)$:

$$\alpha^{\text{compiled}}(t) = \alpha_0^{\text{compiled}}(1 + g^{\text{rep}}(t)), \text{ with } \overline{g^{\text{rep}}(t)} = 0. \tag{5}$$

The blue curve in Fig. 3(B) shows the pulsatility scale factor of the compiled vasculature, $g^{\text{rep}}(t)$, which has a fast rise followed by a slow recovery. Note that the magnitude of $g^{\text{rep}}(t)$ is smaller than $g(t)$ of individual capillaries. Compiling multiple capillaries which have different

phases (i.e. temporal delays) blunts the rise and fall of $g^{\text{rep}}(t)$ but preserves the overall pulsatile variation.

We evaluated Pearson's correlation coefficients among $g(t)$ of individual capillaries and $g^{\text{rep}}(t)$ to characterize: i) the degree of pulsatility synchronization and ii) how well $g^{\text{rep}}(t)$ represents pulsatility of individual capillaries (Fig. 3(C) and (D)). The average correlation coefficient of $g(t)$ with other capillaries is shown in Fig. 3(D). A few individual capillaries showed little correlation with other capillaries. The average correlation of $g^{\text{rep}}(t)$ with the individual capillaries was 0.589.

2.7.4.   Pulsatility compensation in isotropic FOV OCTA protocols

In the 2000 repeated B-scan data set (2.7.3), the 100 ms time window was used to compute $g^{\text{rep}}(t)$ by compiling all vessel voxels in the time window. Here we propose a general method to extract the representative pulsatility for OCTA protocols with isotropic (or near) FOVs and a pulsatility compensation scheme. In OCTA protocols with isotropic FOVs, the slow scan axis encodes both i) time evolution and ii) spatial sweep in the slow scan direction. If we assume the pulsatility is uniform across the FOV, the slow scan direction encodes essentially only time evolution of the pulsatility. Therefore, we propose to measure α over a "band" that covers 100 ms imaging time, treating all vessel voxels in the band as one compiled vasculature, and then slide the band in the slow scan direction to characterize time behavior (Fig. 3(E)). Then, the pulsatility of $\alpha^{\text{band}}(y_n)$, where y_n is the slow scan index of the band, is the representative pulsatility where y_n encodes the time linearly ($t_{\text{imaging}} = y_n N \Delta t$):

$$\alpha^{\text{band}}(y_n) = \alpha_0^{\text{band}}(1 + g^{\text{rep}}(y_n)), \text{ with } \overline{g^{\text{rep}}(y_n)} = 0. \tag{6}$$

The pulsatility compensated $\hat{\alpha}_0$ can be estimated by normalization using Eq. (7):

$$\hat{\alpha}_0(x_n, y_n) = \alpha(x_n, y_n)/(1 + g^{\text{rep}}(y_n)). \tag{7}$$

x_n is the A-scan index in the B-scan. Figure 3(F) shows pulsatility compensation of the DCP. Note this method only compensates the representative pulsatility and does not account for temporal and magnitude heterogeneity of the pulsatility among capillaries. On average, we expect our scheme to under-compensate the pulsatility, because compiling all vessel voxels is expected to reduce the magnitude of pulsatility, as shown in Fig. 3(B). For choroidal vasculature pulsatility compensation, all voxels in the sliding band were treated as compiled vasculature.

2.8.   *Data acquisition for repeatability and consistency evaluation of VISTA measurements*

For repeatability evaluation of the proposed VISTA method, four healthy normal eyes from 4 volunteers (age range from 26 to 40 years old) were imaged with the 3×3 mm protocol. The subjects were instructed to sit back from the instrument headrest and chinrest between repeated acquisitions. Subsequently, the subjects were realigned using a mechanical joystick and refocused using the focus tunable liquid lens. For evaluation of the consistency between VISTA measurements from different protocols, one eye (subject #1) was imaged with the 5×5 mm protocol after the 3×3 mm repeatability protocol image acquisition.

3.   Results

3.1.   *Comparing SCP + ICP and DCP in healthy subjects*

VISTA α measurements in SCP + ICP and DCP from 4 healthy subjects are shown in Fig. 4(A). $\hat{\alpha}_0^{\text{SCP + ICP}}$ and $\hat{\alpha}_0^{\text{DCP}}$ were calculated by averaging $\hat{\alpha}_0(x_n, y_n)$ at vascular skeletons within 1.5 mm eccentricity at each vascular plexus. The subjects were imaged with the 3×3 mm protocol for 4 times (Methods 2.8). In these four subjects, the SCP + ICP showed faster autocorrelation decay

constant than the DCP within the eccentricity of 1.5 mm, for all repeated measurements. The ratios of $\hat{\alpha}_0^{DCP}$ to $\hat{\alpha}_0^{SCP+ICP}$ were ~0.7 and were comparable among the subjects (Fig. 4(B)).
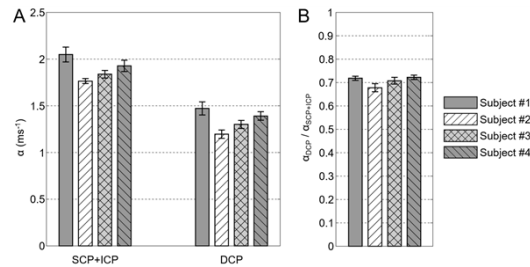

Fig. 4. VISTA α measurements at different plexuses in healthy subjects (age ranging from 26-40 years old).

3.2. Retinal and choroidal vasculature with VISTA

Figure 5 shows VISTA OCTA of 6 different vasculatures from one data set of a healthy subject, imaging the region between the optic nerve head (ONH) and the fovea. Segmentation of the RNFLP, SCP + ICP and DCP are shown in Fig. 5(A). The SCP + ICP has higher α than DCP, and RNFLP has lower α than DCP. Distinct vortex-like and fern-like vascular patterns of DCP are marked with white arrowheads in Fig. 5(B). We observed that the center of these vascular patterns often have high α in VISTA OCTA (arrowheads). Segmentation of three choriocapillaris / choroidal slabs are shown in Fig. 5(C). Slabs 1, 2 and 3 are 13 µm, 27 µm and 40 µm posterior to RPE, respectively. The thickness of the slabs are 8 µm. Slab 1 in en face OCTA shows lobular structures of the choriocapillaris. The centers of several lobules, which have maximal connection to the branches of the lobules, are marked with arrowheads in Fig. 5(E). The same locations are marked in Choroidal slab 2 and show thicker choroidal vessels of ~50 µm diameters. VISTA OCTA of Fig. 5(E) shows that the centers of the lobules have higher α compared to the periphery of the lobules. This suggests that the center of lobular structures have higher blood flow speeds than the periphery of the lobules. Choroidal slab 3 shows a thicker vessel (~150 µm diameter, arrowheads), which has high α in VISTA OCTA (Fig. 5(D)).

3.3. Diabetic retinopathy with VISTA

Representative VISTA OCTA images of the SCP + ICP and DCP of a healthy eye as well as mild, moderate and severe non-proliferative diabetic retinopathy (NPDR) eyes are shown in Fig. 6(A). We observed generally low α in the mild NPDR eye. Figure 6(B) shows an enlargement of the SCP + ICP of the mild NPDR eye from a region with low capillary density. Note the tortuous vessels (arrowheads) and the focal bulge (arrow) have high and low α, respectively. In the moderate NPDR eye, we observed tortuous capillaries which had high α (arrowheads). The severe NPDR eye was anti-VEGF treatment naïve at the time of imaging, and showed high α, even in the DCP. VISTA OCTA images of the SCP + ICP of treated proliferative diabetic retinopathy (PDR) eyes are shown in Fig. 6(C) and (D). Note that even a few thick vessels in Fig. 6(D) have low α (arrowheads). Enlarged views of microvascular lesions such as capillary loops and microaneurysms show that VISTA OCTA provides blood flow speed information that cannot be obtained using standard OCTA. We emphasize that en face OCTA and the 'intensity' (value of HSV) of VISTA OCTA images are derived from unnormalized OCTA, and only the 'color' (hue of HSV) is derived from normalized OCTA and its saturation characteristics.
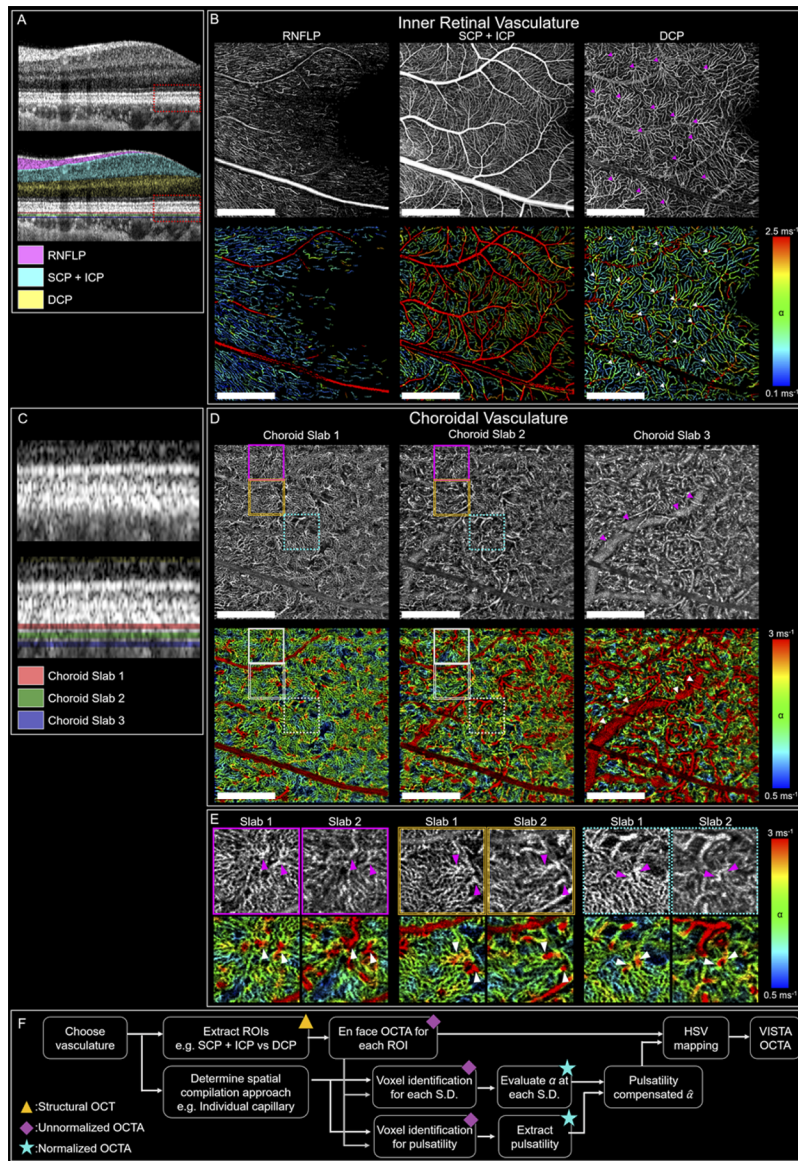
Fig. 5. VISTA OCTA of inner retinal and choroidal vasculature of a healthy subject. (A, C) Segmentation of RNFLP, SCP + ICP, DCP, and Choroidal slabs 1, 2 and 3. (B) En face OCTA (top) and VISTA OCTA (bottom) of RNFLP, SCP + ICP and DCP. Centers of distinct vortex-like and fern-like patterns of DCP are marked with arrowheads, which often show high α in VISTA OCTA. (D) En face OCTA (top) and VISTA OCTA (bottom) of Choroidal slabs 1, 2, and 3. Three boxes in Choroidal slab 1 mark choriocapillaris lobules. The same regions are marked in Choroidal slab 2 to compare vascular structure and flow speeds posterior to the lobules. A thick vessel in Choroidal slab 3 is marked with arrowheads. (E) Enlarged en face OCTA (top) and VISTA OCTA (bottom) of the three boxes in (D). The centers of the choriocapillaris lobules in Choroidal slab 1 are marked with arrowheads, which show high α (left). Thicker choroidal vessels of ~50 μm diameters are posterior to the centers of lobules (right). (F) Flow chart for generating VISTA OCTA. Symbols indicate the type of data used in each step. S.D.: Spatial domain. Scale bars: 1 mm.
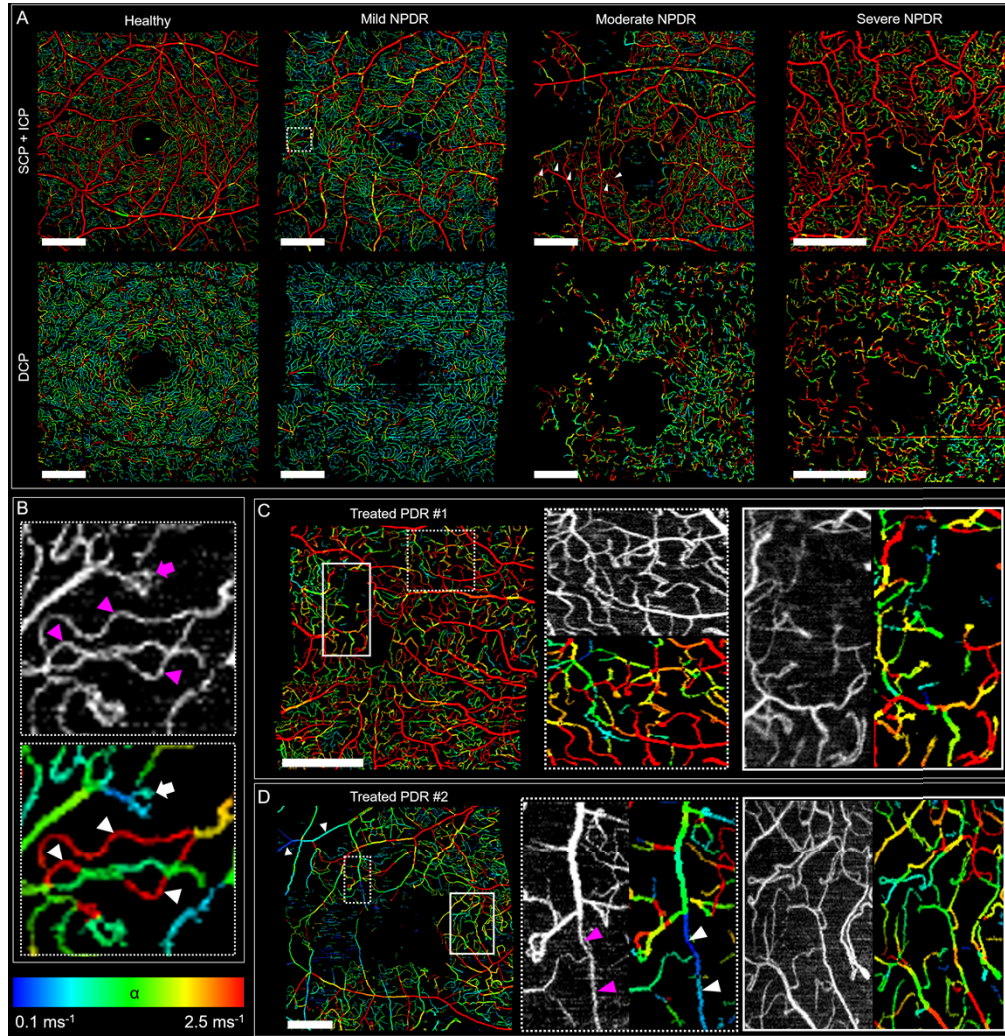
Fig. 6. VISTA OCTA of a representative healthy eye and eyes with different stages of diabetic retinopathy. (A) VISTA OCTA of a healthy eye and eyes with mild, moderate, and severe non-proliferative diabetic retinopathy (NPDR). A dashed box marks the region with low capillary density in the mild NPDR, enlarged in (B). Arrowheads in SCP + ICP of the moderate NPDR mark tortuous capillaries with high α. (B) Arrowheads and an arrow mark the tortuous vessels and the focal bulge. (C, D) VISTA OCTA of treated proliferative DR (PDR) with enlarged views on right. (D) Arrowheads mark the thick vessels (not capillaries) that show low α. Scale bars: 1 mm.

3.4. Repeatability measurements in healthy eyes at the capillary segment level

In order to evaluate repeatability at the capillary segment level, > 100 individual capillary segments from SCP + ICP and DCP, respectively, were manually traced, and the corresponding capillary segments were identified in 4 repeated volumes from subject #1 (healthy). For each segment, $\hat{\alpha}_0(x_n, y_n)$ along the corresponding vascular skeleton was averaged to represent $\hat{\alpha}_0^{\text{segment}}$. Figure 7(A) shows scatter plots of 4 $\hat{\alpha}_0^{\text{segment}}$ measurements. The [mean, median] of coefficient of variance (CV) for individual capillary segment measurements were [0.194, 0.164] for SCP + ICP
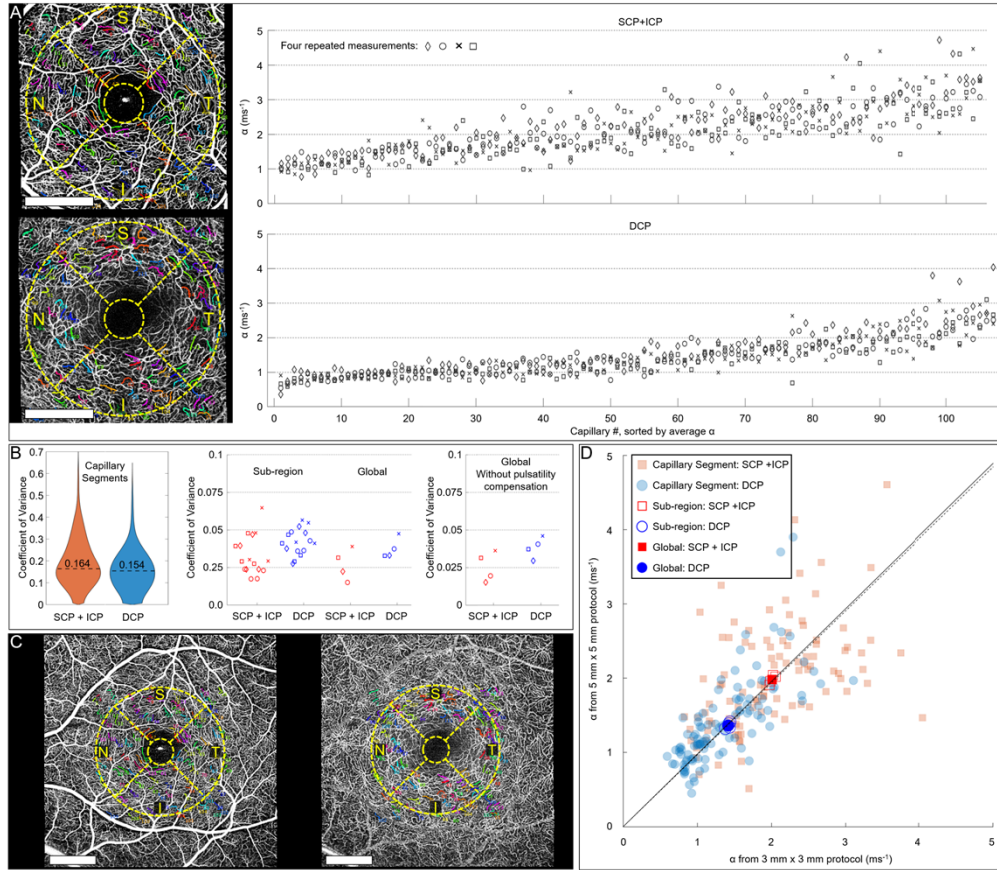
Fig. 7. Repeatability and consistency of VISTA α measurements at different spatial levels. (A) Repeated measurements at the capillary segment level. Color-coded vessels mark the selected capillary segments. Sub-region maps are overlaid on en face OCTA (left). N: Nasal, S: Superior, T: Temporal, I: Inferior. Top row: SCP + ICP. Bottom row: DCP. (B) Coefficient of variance (CV) at different spatial levels. Left: Violin plots of CV of capillary segments. Dashed lines mark medians. Middle and right: Different markers are used for different subjects. Middle: Sub-region includes nasal, superior, temporal and inferior. (C) En face OCTA of 5 mm × 5 mm. Corresponding capillary segments from (A) are color-coded. Left: SCP + ICP. Right: DCP. (D) Comparing α measurements from the 5 mm × 5 mm protocol and the 3 mm × 3 mm protocol at different spatial levels. Scale bars: 1 mm.

and [0.160, 0.154] for DCP. This is comparable to the reported CV of blood flow speeds in retinal capillaries measured using AO [51]. However, note that VISTA measures the temporal autocorrelation decay constant in the vasculature, not the blood flow speed directly.

3.5. Repeatability measurements at the regional level

In order to evaluate repeatability at the regional level, 4 sub-regions (nasal, superior, temporal, inferior) from SCP + ICP and DCP were traced and subsequently identified in 4 repeated volumes each from 4 healthy subjects. For each region, $\hat{\alpha}_0(x_n, y_n)$ at vascular skeletons in the region was averaged to represent $\hat{\alpha}_0^{\text{region}}$. The sum of 4 sub-regions was used to evaluate $\hat{\alpha}_0^{\text{global}}$. The CV of $\hat{\alpha}_0^{\text{region}}$ and $\hat{\alpha}_0^{\text{global}}$ was below 0.075 and 0.05 respectively for both SCP + ICP and DCP and for all subjects (Fig. 7(B)). To examine the dependence of repeatability on pulsatility compensation,

the CV of α_0^{global} without pulsatility compensation was evaluated. The CV was comparable to the case with pulsatility compensation (Fig. 7(B)). This is expected, since the overall effect of pulsatility compensation across FOV will converge to unity and normal healthy subjects do not have local vascular lesions.

3.6. Consistency between different imaging protocols

Depending on the SS-OCT A-scan rate, the FOV, and galvanometer scan speed, the parameters for VISTA OCTA protocols can be different. Since temporal autocorrelation decay fitting and OOF response are the backbone of the new VISTA algorithm, we expect the key parameters to be i) the fundamental interscan time, ii) the number of B-scan repeats and iii) the A-scan spacing. In order for temporal autocorrelation decay constant α measured from VISTA to be a quantitative surrogate marker for blood flow speeds, α measured from different protocols should be consistent, making different VISTA OCTA scan protocols compatible. We imaged subject #1 with both the 3×3 mm and 5×5 mm protocol (Table 1). The capillary segments and regions marked for the repeatability evaluation in the 3×3 mm volume were identified in the 5×5 mm volume (Fig. 7(C)). Figure 7(D) plots the $\hat{\alpha}_0^{\text{segment}}$, $\hat{\alpha}_0^{\text{sub - region}}$ and $\hat{\alpha}_0^{\text{global}}$ measurement from the 3×3 mm protocol on x-axis and the 5×5 mm protocol on y-axis. Note that $\hat{\alpha}_0^{\text{sub - region}}$ and $\hat{\alpha}_0^{\text{global}}$ agree well. To examine the bias (consistent over or under estimation of $\hat{\alpha}_0$) caused by different key parameters, '$y = kx$' was fitted in between the two measurements. Fitting $\hat{\alpha}_0^{\text{segment}}$ and $\hat{\alpha}_0^{\text{region}}$ from the two protocols resulted '$y = 0.969x$' (dashed line in Fig. 7(D)) and '$y = 0.979x$' (solid line) respectively, indicating a small bias between the results from the two scan protocols.

4. Discussion

4.1. Blood flow speed imaging with VISTA

Figure 4 and 5 show that VISTA can enable studies of blood flow speeds in healthy normal retinal vasculature at the capillary level, while still providing multi mm^2 FOV, a scale significantly larger than a few selected vessel segments. To our knowledge, comparing blood flow surrogate markers between the SCP + ICP and DCP has not been reported in humans in vivo. Clear visualization of the lobular structure of choriocapillaris in Fig. 5(E) with high α near the center of the lobules also suggests that VISTA can be applied to assess choriocapillaris flow deficits which are important markers of disease [52–56]. In pathologies such as DR (Fig. 6), focal vascular lesions can be associated with flow markers. Examples are i) correlations between α of capillary segment and their tortuosity, and ii) comparison of α in/near DR lesions to the average α of the plexus. The regional measurements showed high repeatability and compatibility between different OCTA protocols (Fig. 7). Note that VISTA can quantitatively characterize the blood flow speeds using a single global number, such as $\hat{\alpha}_0^{\text{SCP + ICP}}$ or $\hat{\alpha}_0^{\text{DCP}}$, as well as with the distribution of α. The capability of VISTA to provide simple quantitative measurements for an eye, analogous to OCTA vessel density and foveal avascular zone area, simplifies interpretation and can facilitate longitudinal studies on progression or treatment responses.

In addition, we emphasize that the new VISTA protocol still provides standard en face OCTA. This creates a natural connection between future VISTA studies and the existing extensive body of OCTA research. Although a high A-scan rate is required to perform VISTA, smaller FOVs can be assessed using current commercial instruments with 100 to 200 kHz A-scan rates and FOVs can be increased as faster A-scan rates become available.

4.2. Vascular structures where VISTA can be applied

Transverse PSF, interscan time and blood flow speeds in the retina can provide a rough estimate of which vasculature structures can be characterized using OCTA temporal autocorrelation fitting. A 1050 nm beam with 1.4 mm $1/e^2$ diameter, focused with a 17 mm focal length lens assuming

low aberration, produces a calculated PSF of ~16 µm $1/e^2$ beam diameter (~10 µm FWHM) on the retina. Although the optical aberrations of human eyes would make actual transverse PSF on the retina larger, this ideal transverse PSF enables a conservative estimate of which vasculature structures can be characterized using $\rho(\tau)$. In healthy normal subjects, blood flow speeds in thick (>40 µm diameter) vessels have been reported to be >~10 mm/s [57]. With a 1 ms fundamental interscan time, the blood cell displacement between the repeated B-scan will be >~10 µm. Therefore, in transversely oriented thick vessels, $\rho(\tau)$ will be nearly fully decayed even at the shortest interscan time. In this case, where OCTA is nearly fully saturated at $1\Delta t$, the variation in OCTA signal at longer interscan times is likely to be dominated by noise, rather than the actual temporal autocorrelation decay of the vasculature, and fitting $OCTA_{normalized}(\tau) = \beta (1 - \exp(-\alpha\tau))$ will yield a high α. Conversely, blood flow speeds in retinal capillaries are mostly <3 mm/s [7,11,14]. Therefore, we expect the temporal autocorrelation in retinal capillaries to not be fully decayed at short interscan times, and the decay characteristics can be captured by the VISTA algorithm. The beam diameter at pupil can be decreased to enlarge the transverse PSF at retina, varying the maximum blood flow speed that can be characterized with temporal autocorrelation decay, at the cost of transverse image resolution.

4.3. Temporal autocorrelation decay model

Various types of temporal autocorrelation functions, $\rho(\tau)$, in OCT have been suggested for assessing blood flow. Wang et al. approximated the amplitude of backscattered light as a sequence of square pulses and modeled autocorrelation function as $\rho(\tau) = 1 - \alpha'\tau$ when τ is small [21]. The authors experimentally validated a linear relationship between α' and the transverse velocity using intralipid particles. Tokayer et al. demonstrated a linear relationship between normalized OCTA and particle speeds when the interscan time is small, using whole blood flowing in a glass tube [22]. The time range where the linear relationship holds was dependent on the blood flow speeds (i.e. < 0.3 ms for 1.5 mm/s blood flow speed). Note that 1.5 mm/s is in the range of retinal capillary blood flow speeds and 0.3 ms is significantly smaller than the shortest interscan time we used. (The beam $1/e^2$ diameter was 20 µm in the Tokayer et al. study.) Lee et al. proposed a dynamic light scattering OCT which comprehensively modeled the static and noise component of OCT signal [20]. The authors treated diffusion and translational movement of particles separately and the autocorrelation function included a term proportional to $\exp(-\alpha_1\tau - \alpha_2\tau^2)$. Recently, Nam et al. modeled the autocorrelation as $\rho(\tau) = \exp(-\alpha_1{}^2\tau^2)$ and measured pulsatility in thick retinal and choroidal vessels in human retina [23].

Adopting clinically feasible multi mm^2 FOV OCTA protocols limited our choice of temporal autocorrelation function. Even the shortest interscan time of ~1 ms was too long for a linear model, following Tokayer et al. [22]. Because the number of temporal points for $\rho(\tau)$ is limited (<10), models with multiple parameters may lead to overfitting. Therefore, we chose $\rho(\tau) = \exp(-\alpha\tau)$ due to its simplicity and the ease of interpretation of α as temporal autocorrelation decay constant. The single file flow of blood cells and predominantly fixed direction of motion in retinal capillaries may provide guidance on improving the autocorrelation model $\rho(\tau) = \exp(-\alpha\tau)$. Also, it is possible that retinal capillaries and choriocapillaris have different temporal autocorrelation characteristics, since their hemodynamics are different.

4.4. OCT system requirements for VISTA

Assuming that $\rho(\tau) = \exp(-\alpha\tau)$ is a reasonable model for temporal autocorrelation decay in retinal capillaries, the measured α can provide guidance on the fundamental interscan time required for α evaluation using the VISTA algorithm. For example, consider a 3 ms fundamental interscan time using the previous OCT beam size (1.4 mm $1/e^2$ diameter at pupil). At the shortest interscan time, the OCTA signal will already be >99% saturated in the SCP + ICP because the average $\hat{\alpha}_0^{SCP + ICP}$ is ~2 ms^{-1}. We propose using <95% OCTA saturation at the shortest interscan time, or

$\exp(-\alpha\Delta t) > 0.05$, as a phenomenological requirement evaluating the autocorrelation decay. This yields $\alpha_{max}\Delta t_{fundamental} \approx 3$. Assuming the same beam size at the pupil as the previous example, a fundamental interscan time <1.5 ms will be required to characterize the SCP + ICP. Note that the shortest fundamental interscan time achievable is often determined by the characteristics of the galvanometer scanner.

A key advantage of VISTA protocol is that it also generates standard OCTA images, which have been extensively used to study retinal disease. If the maximum interscan time $(N - 1)$ $\Delta t_{fundamental}$ in the OCTA protocol is too short, or α is too small, OCTA will have limited contrast, limiting the VISTA protocol from generating OCTA. We propose >50% saturation of OCTA at the longest interscan time, or $\exp[-\alpha(N-1)\Delta t] < 0.5$, as a requirement for sufficient OCTA contrast. This yields $\alpha_{min}(N - 1)\Delta t_{fundamental} \approx 0.7$.

Finally, fine A-scan spacing is required in order to resolve capillaries for correct spatial compilation and to achieve a large number of samples. If the A-scan spacing is not fine enough, individual capillaries are less likely to be continuously resolved. We have experimentally determined that a $\sim 10\,\mu m$ or finer A-scan spacing is required to robustly resolve retinal capillaries.

The fundamental interscan time and A-scan spacing requirement provide a constraint on the A-scan rate and the maximum FOV for the VISTA protocol. For example, assuming a fundamental interscan time of 1.5 ms, $10\,\mu m$ A-scan spacing, and 75% scanner duty cycle, a ~ 530 kHz A-scan rate will be required to achieve 6 mm FOV in the fast scan direction. The A-scan rate requirement can be reduced linearly by sacrificing the fast scan FOV. Montaging, anisotropic FOVs, using a smaller beam diameter at the pupil, and improving the scanner duty cycle can also further reduce the A-scan rate requirement.

4.5. Spatial compilation approaches

The capillary segment spatial compilation approach was motivated by the distinct layered structure of inner retinal vasculature and blood flow speed changes at capillary bifurcation points. Note that grouping SCP and ICP together as proposed can decrease the scale of spatial compilation. If two capillaries in SCP + ICP cross each other at different depth locations, the capillaries would be divided into sub-segments during the pixel level capillary segmentation from en face OCTA (Fig. 1(A)), reducing the number of voxels for the spatial compilation.

Alternate spatial compilation approaches are also possible. For example, the radial peripapillary capillary near the ONH has a radial orientation. Therefore, disc sectors defined by the angle from the ONH can be used for spatial compilation. Different spatial compilation methods may be needed to assess focal vascular lesions. For example, microaneurysms can be inaccurately segmented if the target radius of OOF is smaller than the size of microaneurysms or the 2D vesselness filter does not have high sensitivity to spherical structures. In these cases, different segmentation methods, such as deep-learning, can be used to detect microvascular lesions and determine the appropriate spatial domain for OCTA compilation. However, a chosen spatial domain needs to support the sufficiently large numbers of samples. If the domain does not have enough voxels, the saturation characteristic of the domain may be dominated by noise.

4.6. Limitations to pulsatility compensation

If there is eye motion or blinking, the pulsatility compensation may introduce artifacts which will limit OCTA compilation from the sliding band in the slow scan direction (Fig. 3(E)). Using the sliding band with a longer imaging time window may make evaluation of α^{band} more robust, at the cost of reduced time resolution. Also, our pulsatility compensation scheme assumes the same degree of pulsatility across FOV, which may not hold true if there are local lesions such as edema. Cardiac-gated multiple OCTA acquisitions can be used to reconstruct the pulsatile flow variations at all positions in the FOV [17]. However, this requires longer acquisition times and large datasets.

5. Conclusion

We developed and demonstrated a second generation VISTA OCTA algorithm that provides a quantitative surrogate marker for blood flow speeds. SS-OCT with a 600 kHz A-scan rate enabled clinically feasible imaging protocols with fine A-scan spacing over multi mm^2 FOV and short interscan times (~1 ms), within a total acquisition time of 3.6 s. Compiled normalized OCTA measurements at multiple interscan times were fitted to a temporal autocorrelation decay model to evaluate a temporal autocorrelation decay constant α. Fine A-scan spacing facilitated capillary identification at individual capillary segment level for spatial compilation of OCTA. VISTA OCTA measured α showed pulsatility in retinal capillaries consistent with the previous AO measurements, and a pulsatility compensation scheme was demonstrated. We evaluated repeatability of VISTA OCTA and consistency of α measurements from different imaging protocols at multiple spatial levels. We observed blood flow speed differences among retinal vascular plexuses in healthy eyes and blood flow speed alterations in eyes with DR. Finally, OCT system requirements for VISTA and different spatial compilation tactics were discussed. These advances promise to enable clinical studies of blood flow speed alterations in diseases such as diabetes and diabetic retinopathy, providing earlier markers of disease, progression and response to therapy.

References

1. C. J. Pournaras, E. Rungger-Brändle, C. E. Riva, S. H. Hardarson, and E. Stefansson, "Regulation of retinal blood flow in health and disease," Prog. Retinal Eye Res. **27**(3), 284–330 (2008).
2. J. Kur, E. A. Newman, and T. Chan-Ling, "Cellular and physiological mechanisms underlying blood flow regulation in the retina and choroid in health and disease," Prog. Retinal Eye Res. **31**(5), 377–406 (2012).
3. A. Daruich, A. Matet, A. Moulin, L. Kowalczuk, M. Nicolas, A. Sellam, P.-R. Rothschild, S. Omri, E. Gélizé, L. Jonet, K. Delaunay, Y. D. Kozka, M. Berdugo, M. Zhao, P. Crisanti, and F. Behar-Cohen, "Mechanisms of macular edema: beyond the surface," Prog. Retinal Eye Res. **63**, 20–68 (2018).
4. J. Penn, A. Madan, R. B. Caldwell, M. Bartoli, R. Caldwell, and M. Hartnett, "Vascular endothelial growth factor in eye disease," Prog. Retinal Eye Res. **27**(4), 331–371 (2008).
5. J. Tang and T. S. Kern, "Inflammation in diabetic retinopathy," Prog. Retinal Eye Res. **30**(5), 343–358 (2011).
6. A. W. Stitt, T. M. Curtis, M. Chen, R. J. Medina, G. J. McKay, A. Jenkins, T. A. Gardiner, T. J. Lyons, H.-P. Hammes, R. Simo, and N. Lois, "The progress in understanding and treatment of diabetic retinopathy," Prog. Retinal Eye Res. **51**, 156–186 (2016).
7. S. A. Burns, A. E. Elsner, and T. J. Gast, "Imaging the retinal vasculature," Annu. Rev. Vis. Sci. **7**(1), 129–153 (2021).
8. S. Yazdanfar, A. M. Rollins, and J. A. Izatt, "Imaging and velocimetry of the human retinal circulation with color Doppler optical coherence tomography," Opt. Lett. **25**(19), 1448–1450 (2000).
9. Y. Wang, B. A. Bower, J. A. Izatt, O. Tan, and D. Huang, "In vivo total retinal blood flow measurement by Fourier domain Doppler optical coherence tomography," J. Biomed. Opt. **12**(4), 041215 (2007).
10. C. E. Riva, E. Logean, and B. Falsini, "Visually evoked hemodynamical response and assessment of neurovascular coupling in the optic nerve and retina," Prog. Retinal Eye Res. **24**(2), 183–215 (2005).

11. S. A. Burns, A. E. Elsner, K. A. Sapoznik, R. L. Warner, and T. J. Gast, "Adaptive optics imaging of the human retina," Prog. Retinal Eye Res. **68**, 1–30 (2019).
12. R. L. Warner, A. de Castro, L. Sawides, T. Gast, K. Sapoznik, T. Luo, and S. A. Burns, "Full-field flicker evoked changes in parafoveal retinal blood flow," Sci. Rep. **10**, 1–10 (2020).
13. A. de Castro, G. Huang, L. Sawides, T. Luo, and S. A. Burns, "Rapid high resolution imaging with a dual-channel scanning technique," Opt. Lett. **41**(8), 1881–1884 (2016).
14. B. Gu, X. Wang, M. D. Twa, J. Tam, C. A. Girkin, and Y. Zhang, "Noninvasive in vivo characterization of erythrocyte motion in human retinal capillaries using high-speed adaptive optics near-confocal imaging," Biomed. Opt. Express **9**(8), 3653–3677 (2018).
15. P. Bedggood and A. Metha, "Mapping flow velocity in the human retinal capillary network with pixel intensity cross correlation," PLoS One **14**(6), e0218918 (2019).
16. P. Bedggood and A. Metha, "Direct measurement of pulse wave propagation in capillaries of the human retina," Opt. Lett. **46**(18), 4450–4453 (2021).
17. B. Lee, W. Choi, J. J. Liu, C. D. Lu, J. S. Schuman, G. Wollstein, J. S. Duker, N. K. Waheed, and J. G. Fujimoto, "Cardiac-gated en face Doppler measurement of retinal blood flow using swept-source optical coherence tomography at 100,000 axial scans per second," Invest. Ophthalmol. Visual Sci. **56**(4), 2522–2530 (2015).
18. R. Haindl, W. Trasischker, A. Wartak, B. Baumann, M. Pircher, and C. K. Hitzenberger, "Total retinal blood flow measurement by three beam Doppler optical coherence tomography," Biomed. Opt. Express **7**(2), 287–301 (2016).
19. W. Trasischker, R. M. Werkmeister, S. Zotter, B. Baumann, T. Torzicky, M. Pircher, and C. K. Hitzenberger, "In vitro and in vivo three-dimensional velocity vector measurement by three-beam spectral-domain Doppler optical coherence tomography," J. Biomed. Opt. **18**(11), 116010 (2013).
20. J. Lee, W. Wu, J. Y. Jiang, B. Zhu, and D. A. Boas, "Dynamic light scattering optical coherence tomography," Opt. Express **20**(20), 22262–22277 (2012).
21. Y. Wang and R. Wang, "Autocorrelation optical coherence tomography for mapping transverse particle-flow velocity," Opt. Lett. **35**(21), 3538–3540 (2010).
22. J. Tokayer, Y. Jia, A.-H. Dhalla, and D. Huang, "Blood flow velocity quantification using split-spectrum amplitude-decorrelation angiography with optical coherence tomography," Biomed. Opt. Express **4**(10), 1909–1924 (2013).
23. A. S. Nam, B. Braaf, and B. J. Vakoc, "Using the dynamic forward scattering signal for optical coherence tomography based blood flow quantification," Opt. Lett. **47**(12), 3083–3086 (2022).
24. J. G. Fujimoto and D. Huang, "Foreword: 25 years of optical coherence tomography," Invest. Ophthalmol. Visual Sci. **57**, OCTi–OCTii (2016).
25. D. Huang, E. A. Swanson, C. P. Lin, J. S. Schuman, W. G. Stinson, W. Chang, M. R. Hee, T. Flotte, K. Gregory, and C. A. Puliafito, "Optical coherence tomography," Science **254**(5035), 1178–1181 (1991).
26. I. Laíns, J. C. Wang, Y. Cui, R. Katz, F. Vingopoulos, G. Staurenghi, D. G. Vavvas, J. W. Miller, and J. B. Miller, "Retinal applications of swept source optical coherence tomography (OCT) and optical coherence tomography angiography (OCTA)," Prog. Retinal Eye Res. **84**, 100951 (2021).
27. R. F. Spaide, J. G. Fujimoto, N. K. Waheed, S. R. Sadda, and G. Staurenghi, "Optical coherence tomography angiography," Prog. Retinal Eye Res. **64**, 1–55 (2018).
28. T. T. Hormel, Y. Jia, Y. Jian, T. S. Hwang, S. T. Bailey, M. E. Pennesi, D. J. Wilson, J. C. Morrison, and D. Huang, "Plexus-specific retinal vascular anatomy and pathologies as seen by projection-resolved optical coherence tomographic angiography," Prog. Retinal Eye Res. **80**, 100878 (2021).
29. T. S. Hwang, Y. Jia, S. S. Gao, S. T. Bailey, A. K. Lauer, C. J. Flaxel, D. J. Wilson, and D. Huang, "Optical coherence tomography angiography features of diabetic retinopathy," Retina **35**(11), 2371–2376 (2015).
30. S. Parrulli, F. Corvi, M. Cozzi, D. Monteduro, F. Zicarelli, and G. Staurenghi, "Microaneurysms visualisation using five different optical coherence tomography angiography devices compared to fluorescein angiography," Br. J. Ophthalmol. **105**(4), 526–530 (2021).
31. A. Couturier, V. Mané, S. Bonnin, A. Erginay, P. Massin, A. Gaudric, and R. Tadayoni, "Capillary plexus anomalies in diabetic retinopathy on optical coherence tomography angiography," Retina **35**(11), 2384–2391 (2015).
32. Y. Jia, S. T. Bailey, D. J. Wilson, O. Tan, M. L. Klein, C. J. Flaxel, B. Potsaid, J. J. Liu, C. D. Lu, M. F. Kraus, J. G. Fujimoto, and D. Huang, "Quantitative optical coherence tomography angiography of choroidal neovascularization in age-related macular degeneration," Ophthalmology **121**(7), 1435–1444 (2014).
33. S. A. Agemy, N. K. Scripsema, C. M. Shah, T. Chui, P. M. Garcia, J. G. Lee, R. C. Gentile, Y.-S. Hsiao, Q. Zhou, T. Ko, and R. B. Rosen, "Retinal vascular perfusion density mapping using optical coherence tomography angiography in normals and diabetic retinopathy patients," Retina **35**(11), 2353–2363 (2015).
34. E. Talisa, A. T. Chin, M. A. Bonini Filho, M. Adhi, L. Branchini, D. A. Salz, C. R. Baumal, C. Crawford, E. Reichel, and A. J. Witkin, "Detection of microvascular changes in eyes of patients with diabetes but not clinical diabetic retinopathy using optical coherence tomography angiography," Retina **35**, 2364–2370 (2015).
35. B. Dupas, W. Minvielle, S. Bonnin, A. Couturier, A. Erginay, P. Massin, A. Gaudric, and R. Tadayoni, "Association between vessel density and visual acuity in patients with diabetic retinopathy and poorly controlled type 1 diabetes," JAMA Ophthalmol. **136**(7), 721–728 (2018).
36. T. S. Hwang, S. S. Gao, L. Liu, A. K. Lauer, S. T. Bailey, C. J. Flaxel, D. J. Wilson, D. Huang, and Y. Jia, "Automated quantification of capillary nonperfusion using optical coherence tomography angiography in diabetic retinopathy," JAMA Ophthalmol. **134**(4), 367–373 (2016).

37. W. Choi, E. M. Moult, N. K. Waheed, M. Adhi, B. Lee, C. D. Lu, E. Talisa, V. Jayaraman, P. J. Rosenfeld, J. S. Duker, and J. G. Fujimoto, "Ultrahigh-speed, swept-source optical coherence tomography angiography in nonexudative age-related macular degeneration with geographic atrophy," Ophthalmology **122**(12), 2532–2544 (2015).

38. S. B. Ploner, E. M. Moult, W. Choi, N. K. Waheed, B. Lee, E. A. Novais, E. D. Cole, B. Potsaid, L. Husvogt, J. Schottenhamml, A. Maier, P. J. Rosenfeld, J. S. Duker, J. Hornegger, and J. G. Fujimoto, "Toward quantitative optical coherence tomography angiography: visualizing blood flow speeds in ocular pathology using variable interscan time analysis," Retina **36**(Supplement 1), S118–S126 (2016).

39. C. B. Rebhun, E. M. Moult, E. A. Novais, C. Moreira-Neto, S. B. Ploner, R. N. Louzada, B. Lee, C. R. Baumal, J. G. Fujimoto, J. S. Duker, N. K. Waheed, and D. Ferrara, "Polypoidal choroidal vasculopathy on swept-source optical coherence tomography angiography with variable interscan time analysis," Trans. Vis. Sci. Techol. **6**(6), 4 (2017).

40. M. Arya, M. Bonini Filho, C. B. Rebhun, E. M. Moult, B. Lee, Y. Alibhai, A. J. Witkin, C. R. Baumal, J. S. Duker, J. G. Fujimoto, and N. K. Waheed, "Analyzing relative flow speeds in diabetic retinopathy using variable interscan time analysis OCT angiography," Ophthalmol. Retina **5**(1), 49–59 (2021).

41. C. B. Rebhun, E. M. Moult, S. B. Ploner, C. M. Neto, A. Y. Alibhai, J. Schottenhamml, B. Lee, W. Choi, F. A. Rifai, M. W. Tam, L. Husvogt, C. R. Baumal, A. J. Witkin, A. Maier, P. J. Rosenfeld, J. S. Duker, J. G. Fujimoto, and N. K. Waheed, "Analyzing relative blood flow speeds in choroidal neovascularization using variable interscan time analysis OCT angiography," Ophthalmol. Retina **2**(4), 306–319 (2018).

42. W. Choi, N. K. Waheed, E. M. Moult, M. Adhi, B. Lee, T. De Carlo, V. Jayaraman, C. R. Baumal, J. S. Duker, and J. G. Fujimoto, "Ultrahigh speed swept source optical coherence tomography angiography of retinal and choriocapillaris alterations in diabetic patients with and without retinopathy," Retina **37**(1), 11–21 (2017).

43. American National Standards Institute, "Ophthalmics - Light Hazard Protection For Ophthalmic Instruments," in *ANSI Z80.36* (American National Standards Institute, 2021).

44. Y. Jia, O. Tan, J. Tokayer, B. Potsaid, Y. Wang, J. J. Liu, M. F. Kraus, H. Subhash, J. G. Fujimoto, J. Hornegger, and D. Huang, "Split-spectrum amplitude-decorrelation angiography with optical coherence tomography," Opt. Express **20**(4), 4710–4725 (2012).

45. M. Guizar-Sicairos, S. T. Thurman, and J. R. Fienup, "Efficient subpixel image registration algorithms," Opt. Lett. **33**(2), 156–158 (2008).

46. Y. Jia, J. M. Simonett, J. Wang, X. Hua, L. Liu, T. S. Hwang, and D. Huang, "Wide-field OCT angiography investigation of the relationship between radial peripapillary capillary plexus density and nerve fiber layer thickness," Invest. Ophthalmol. Visual Sci. **58**(12), 5188–5194 (2017).

47. J. Lee, J. Y. Jiang, W. Wu, F. Lesage, and D. A. Boas, "Statistical intensity variation analysis for rapid volumetric imaging of capillary network flux," Biomed. Opt. Express **5**(4), 1160–1172 (2014).

48. T. Jerman, F. Pernuš, B. Likar, and Ž. Špiclin, "Enhancement of vascular structures in 3D and 2D angiographic images," IEEE Trans. Med. Imaging **35**(9), 2107–2118 (2016).

49. P. Kollmannsberger, M. Kerschnitzki, F. Repp, W. Wagermaier, R. Weinkamer, and P. Fratzl, "The small world of osteocytes: connectomics of the lacuno-canalicular network in bone," New J. Phys. **19**(7), 073019 (2017).

50. M. W. Law and A. C. Chung, "Three dimensional curvilinear structure detection using optimally oriented flux," in *Computer Vision–ECCV 2008: 10th European Conference on Computer Vision*, Marseille, France, October 12-18, 2008, Proceedings, Part IV 10 (Springer, 2008), pp. 368–382.

51. R. L. Warner, T. J. Gast, K. A. Sapoznik, A. Carmichael-Martins, and S. A. Burns, "Measuring temporal and spatial variability of red blood cell velocity in human retinal vessels," Invest. Ophthalmol. Visual Sci. **62**(14), 29 (2021).

52. F. Corvi, L. Tiosano, G. Corradetti, M. G. Nittala, S. Lindenberg, A. R. Alagorie, J. A. McLaughlin, T. K. Lee, and S. R. Sadda, "Choriocapillaris flow deficits as a risk factor for progression of age-related macular degeneration," Retina **41**(4), 686–693 (2021).

53. M. Thulliez, Q. Zhang, Y. Shi, H. Zhou, Z. Chu, L. de Sisternes, M. K. Durbin, W. Feuer, G. Gregori, and R. K. Wang, "Correlations between choriocapillaris flow deficits around geographic atrophy and enlargement rates based on swept-source OCT imaging," Ophthalmol. Retina **3**(6), 478–488 (2019).

54. E. M. Moult, N. K. Waheed, E. A. Novais, W. Choi, B. Lee, S. B. Ploner, E. D. Cole, R. N. Louzada, C. D. Lu, P. J. Rosenfeld, J. S. Duker, and J. G. Fujimoto, "Swept-source optical coherence tomography angiography reveals choriocapillaris alterations in eyes with nascent geographic atrophy and drusen-associated geographic atrophy," Retina **36**(Supplement 1), S2–S11 (2016).

55. Q. Zhang, F. Zheng, E. H. Motulsky, G. Gregori, Z. Chu, C.-L. Chen, C. Li, L. De Sisternes, M. Durbin, P. J. Rosenfeld, and R. K. Wang, "A novel strategy for quantifying choriocapillaris flow voids using swept-source OCT angiography," Invest. Ophthalmol. Visual Sci. **59**(1), 203–211 (2018).

56. R. F. Spaide, "Choriocapillaris flow features follow a power law distribution: implications for characterization and mechanisms of disease progression," Am. J. Ophthalmol. **170**, 58–67 (2016).

57. C. M. A. Palochak, H. E. Lee, J. Song, A. Geng, R. A. Linsenmeier, S. A. Burns, and A. A. Fawzi, "Retinal blood velocity and flow in early diabetes and diabetic retinopathy using adaptive optics scanning laser ophthalmoscopy," J. Clin. Med. **8**(8), 1165 (2019).